Building better all-solid-state batteries with Li-garnet solid electrolytes and metalloid anodes

Author(s):
Afyon, Semih; Kravchyk, Kostiantyn V.; Wang, Shutao; van den Broek, Jan; Hänsel, Christian; Kovalenko, Maksym V.; Rupp, Jennifer L.M.

Publication date:
2019-10-07

Permanent link:
https://doi.org/10.3929/ethz-b-000372251

Originally published in:
Journal of Materials Chemistry A 7(37), https://doi.org/10.1039/c9ta04999a

Journal of Materials Chemistry A

PAPER

View Article Online
View Journal | View Issue

Cite this: J. Mater. Chem. A, 2019, 7, 21299

Building better all-solid-state batteries with Li-garnet solid electrolytes and metalloid anodes†‡

Semih Afyon, §*[a] Kostiantyn V. Kravchyk, §[bc] Shutao Wang, §[bc] Jan van den Broek,[a] Christian Hänsel,[a] Maksym V. Kovalenko *[bc] and Jennifer L. M. Rupp*[ade]

All-solid-state batteries provide new opportunities to realize safe, non-flammable, and temperature-tolerant energy storage and display a huge potential to be the core of future energy storage devices, especially in applications where energy density is key to the technology. Garnet-type solid-state electrolytes based on cubic $Li_7La_3Zr_2O_{12}$ possess one of the highest Li^+ conductivities, a wider electrochemical stability window compared to liquid electrolytes, and exceptional chemical and thermal stabilities among various solid electrolytes. Most of the first reports, however, employ lithium metal as the anode with unavoidable Li-dendrite formation through polycrystalline Li-garnet electrolytes at current densities above 0.5 mA cm^{-2}. Accordingly, alternative materials and processing strategies for anodes or interlayers are inherently needed for high currents and fast charging for Li-garnet-type battery integration. Here, we demonstrate, through the use of a composite anode based on antimony nanocrystals, that metalloids offer high and stable storage capacities of up to 330 mA h g^{-1} for Li-garnet all-solid-state batteries at reasonably high current densities (*e.g.* 240 mA g^{-1}) at 95 °C. The results are also compared towards standard liquid type electrolytes and reveal high coulombic efficiencies and improved cycle stability for the solid-state cell design. Guidelines and aspects to process alternative materials and impact the interface design towards fast lithium charge transfer between the metalloid and the Li-garnet electrolyte are formulated. The architecture and scalable processing of metalloid-based batteries are obvious advantages of this work, opening a promising avenue to avoid Li-dendrite formation at high current loads in garnet-type all-solid-state rechargeable batteries.

Received 13th May 2019
Accepted 1st September 2019

DOI: 10.1039/c9ta04999a

rsc.li/materials-a

1. Introduction

Li-ion batteries (LIBs) are the most popular energy storage technology for electric vehicles and consumer electronics due to their long cycle life at high energy and power density.[1–3] However, state-of-the-art LIBs contain flammable liquid electrolytes, which limit their safety and reliable operation window with regards to their operation temperature and potential. These problems challenge scientists to develop new materials and processing routes to provide safe battery architectures by controlling or eliminating thermal runway hazards (explosion),[4,5] detrimental propagation of Li-dendrites,[6] or leakage[2] without increasing total battery weight. Replacing liquid-based electrolytes with innovative solid-state superionic conductors allows the active modulation of electrochemical, mechanical and thermal stability to assure high safety compared to classic polymers or ionic liquids. Such solid-state lithium-ion batteries (SSLIBs) may also allow the use of high capacity cathodes such as sulphur-,[7] manganese-,[8,9] and vanadate-based[9,10] electrode materials or even Li-metal anodes[11] with promising cycle lifetimes.[12,13] Miniaturization and fabrication of the battery components such as thin film microbatteries enables further applications, in particular, small autonomous devices such as sensors for the Internet of Things (IoT).[14] Nevertheless, despite the advantages of SSLIBs, their cycling lifetime and performance must be improved to allow applications in electric vehicles and other devices. More so, increasing battery life cycles is an important goal for socio-economic world peace in order to decrease the capital cost of

[a]ETH Zurich, Electrochemical Materials, Department of Materials, CH-8093 Zurich, Switzerland. E-mail: semih.afyon@alumni.ethz.ch

[b]ETH Zurich, Department of Chemistry and Applied Biosciences, CH-8093 Zurich, Switzerland. E-mail: mvkovalenko@ethz.ch

[c]Laboratory for Thin Films and Photovoltaics, Empa – Swiss Federal Laboratories for Materials Science and Technology, Überlandstrasse 129, CH-8600 Dübendorf, Switzerland

[d]Electrochemical Materials, Department of Materials Science and Engineering, Massachusetts Institute of Technology, 77 Massachusetts Av., MA, 02139, USA. E-mail: jrupp@mit.edu

[e]Electrochemical Materials, Department of Electrical Engineering and Computer Science, Massachusetts Institute of Technology, 77 Massachusetts Av., Cambridge, MA, 02139, USA

† Dedicated to Professor Reinhard Nesper on the occasion of his 70th birthday.

‡ Electronic supplementary information (ESI) available. See DOI: 10.1039/c9ta04999a

§ S. Afyon, K. Kravchyk and S. Wang should be considered co-first authors.

energy storage and to be resourceful with the elements of lithium and potential conflict-element cobalt often used in cathodes today.[15–18]

State-of-the-art SSLIBs exhibit a simple solidified assembly of a cathode, electrolyte and anode. Among the plethora of solid lithium electrolyte materials investigated, engineering fast lithium superionic conductors with a high electrochemical stability voltage window remains a formidable challenge.[4,19] For example, the electrolytes $Li_{10}GeP_2S_{12}$ with high ionic conductivity of 12 mS cm^{-1} at RT,[20] $Li_{3.25}Ge_{0.25}P_{0.75}S_4$ (2.2 mS cm^{-1} at RT)[21] and $Li_7P_3S_{11}$ glass-ceramics (17 mS cm^{-1} at RT)[22] exhibit only a narrow voltage window with electrochemical stability[23] and limited chemical stability in contact with Li-metal anodes[24–26] despite their fast conduction. Attempts to reduce their low stability, particularly towards the electrodes, by protective layers such as In–Li alloy[27] on the anode side or NiS,[28] $Li_4Ti_5O_{12}$,[29] $LiNbO_3$,[30] or $BaTiO_3$ (ref. 31) on the cathode side may increase cycle life time, but at the expense of increased gravimetric energy density and cost. Recently, lithium solid electrolytes of the garnet family such as $Li_7La_3Zr_2O_{12}$ (LLZO) have gained attention, exhibiting a substantially increased electrochemical operation window of 0 to 6 V *vs.* Li^+/Li[32] at high Li-ion conductivity of up to 1 mS cm^{-1}.[33,34] For these ceramic electrolytes, the desired fast conducting cubic phase can be stabilized by a variety of dopants (*e.g.* Al^{3+},[35–44] Ga^{3+},[35,41,45–49]) resulting in stability at increased temperatures (*e.g.* 20–900 °C (ref. 33)) and good chemical compatibility with metallic Li.[11,33,50] LLZO can be readily synthesized by a modified sol–gel combustion reaction (as shown for Ga-[45] and Al-doped LLZO[51]) resulting in sub-micron particles. Because of the small particle size and therefore high sintering activity of the powder, LLZO pellets with high relative densities and high Li-ion conductivities can be sintered at relatively lower temperatures in comparison to classical syntheses (*e.g.* solid-state powder[52] and sol–gel[53] methods). Even though investigations and literature on the synthesis, physical, and chemical properties of this interesting solid inorganic electrolyte are vast,[34,54] reports on the stability of LLZO with anode materials especially at high current rates are still scarce. Without any doubt the application of a Li-metal anode is desired for substantially increasing energy density, and progress was made in reducing the high interfacial resistance between Li-metal anode and solid electrolyte by a variety of different interface layers.[55–57] However, recent studies have shown a clear evidence for the formation of Li-dendrites and structural defects at increased current densities.[58] For example, lithium electroplates and penetrates as dendrites in the pores, cavities,[59] and grain boundaries[60] of LLZO at current densities exceeding 0.5 mA cm^{-2},[59–63] finally leading to an abrupt battery failure and a short circuit. Such low current densities correspond to slow and rather impractical charging times (10 to 20 hours). In this regard, alternatives to Li-metal anode materials or electrolyte/electrode interlayers and their stability with garnet-type LLZO electrolyte must be investigated. Viable alternatives may include the use of oxide-materials or other metals for the anodes. Very recently, various processing strategies and close to theoretical capacities of up to ~175 A h kg^{-1} using $Li_4Ti_5O_{12}$ anode materials with LLZO for SSLIBs were successfully demonstrated.[51,64,65] To further extend the capacity of the anode and, at the same, to avoid the propagation of lithium dendrites at high currents we turn in this work to the anodes made of metalloids for LLZO batteries. It is known from previous studies of LIBs that Sb, Sn, and Si are highly promising anode materials due to their high capacities (660 mA h g^{-1} for Sb,[66,67] 992 mA h g^{-1} for Sn[68–71] and 4200 mA h g^{-1} for Si[72,73]) and relatively low charging voltages of ~1, 0.8, and 0.5 V, respectively. These metalloid anodes form alloys with lithium (*i.e.* Li_3Sb, $Li_{22}Sn_5$ and $Li_{15}Si_4$) involving drastic volumetric changes up to 310% upon their full lithiation resulting in structural and cyclic instabilities of bulk samples; among those, Sb is a less demanding metalloid showing the highest cyclic stability when nanostructured for LIBs primarily due to relatively small volume expansion (135%)[66–69,74] and fast rate capability through limited intermediate crystalline phases.[75,76] Despite these promising properties, integration of antimony anodes into SSLIBs based on LLZO garnet electrolytes have so far not been undertaken.

Here, we show that alloying type metalloids such as antimony can be considered as alternative anodes for SSLIBs based on solid garnet-type electrolytes offering increased energy density and cycling stability. In such a battery configuration, all interfaces are solid-state and potential lithium plating/stripping instabilities and dendrite formation can intrinsically be avoided by replacing Li with Sb. In the battle for affordable energy storage, we purposely focus in the processing of the solid-state battery with the garnet and antimony components on mass-manufacturable and inexpensive solution (slurry) processing of the anode comprised of Sb nanoparticles, carbon black, LLZO particles and polyvinylidene fluoride binder and demonstrate co-assembly with a solid-state Li-garnet electrolyte at the battery cell level. Within the plethora of all-solid-state battery avoiding any type of liquids in cells, we demonstrate with these simple and industrially scalable architectures high storage capacities of up to 330 mA h g^{-1} with stable cycling for the garnet-type batteries. Further, the performance of such all-solid-state batteries is directly compared to batteries with the same electrode configuration employing the state-of-the-art liquid electrolytes. We take advantage of the high theoretical capacity for metalloid anodes to cycle Li-garnet solid-state batteries without any intrinsic risk for Li-dendrites and demonstrate processing guidelines and high performances for functional all-solid-state batteries.

2. Results and discussion

Garnet-type solid electrolytes with a composition of c-$Li_{6.25}Al_{0.25}La_3Zr_2O_{12}$ (LLZO) are used for the composite electrode and the all-solid-state battery cell configurations. The synthesis of the c-$Li_{6.25}Al_{0.25}La_3Zr_2O_{12}$ is based on a modified sol–gel synthesis-combustion method resulting in sub-micron-sized particles after calcination at a low temperature of 650 °C.[51] c-$Li_{6.25}Al_{0.25}La_3Zr_2O_{12}$ solid electrolyte pellets with relative densities of ~87 ± 3% and ionic conductivities of ~0.5 × 10^{-3} S cm^{-1} (RT) have been produced from this powder that are used to construct the all-solid-state Li-ion batteries.[51,64] A slurry

comprising Sb nanoparticles (NPs), LLZO electrolyte powder, carbon black, and PVDF was tape-casted onto sintered thin (300–400 μm) LLZO pellets. The dried composite electrodes were then isostatically pressed at 1000 kN onto the solid electrolyte in order to ensure a good contact at the LLZO/electrode interface (see Fig. 1 and Experimental section for further details). This processing method is both inexpensive and scalable. The solid-state half-cell consisting of the composite Sb-based working electrode prior to the attachment of the metallic lithium as counter and reference electrode is shown in Fig. 2. To overcome the instability issues of the Sb anode during its lithiation/de-lithiation and to ensure the efficient mixing of active material with the sub-micron sized LLZO, Sb has been employed in the form of nanoparticles (Fig. 2a) using an industrially scalable synthesis method based on the reduction of antimony chloride in *N*-methyl-2-pyrrolidone (NMP) solvent by sodium borohydride (see ref. 77 for details). After isostatic pressing of the composite electrode, its final thickness is *ca.* 10 μm showing good mechanical adhesion to the LLZO solid-state electrolyte surface as displayed in Fig. 2b and c. Isostatic pressing is an important prerequisite to assure good mechanical contact and also to ensure enhanced ionic transference as previously shown for similarly prepared cells with $Li_4Ti_5O_{12}$ anodes.[64] Here, the integration of the composite-electrode into the solid electrolyte is also seemingly effective as no peeling from the ceramic pellet is visible and no clear distinction line at the solid electrolyte/electrode interface could be observed (Fig. 2b and c). The composite electrode is a continuously graded structure throughout the cell and it is also densely compacted, assuring a good contact between the different electrode constituents. To ensure that no additional crystalline phases form during the processing steps (*e.g.* by ball-milling, slurry preparation, casting, drying, and pressing steps), powder XRD patterns of the dried Sb/LLZO/C/PVDF composite electrode were analyzed. As seen in the Fig. 2d, no additional crystalline products were observed besides the main electrode Sb phase and the electrolyte being in cubic $Li_{6.25}Al_{0.25}La_3Zr_2O_{12}$ phase. This observation also confirms the absence of any chemical reaction of Sb nanoparticles with LLZO electrolyte and also towards NMP solvent and PVDF binder involved during the preparation steps.

To test and discuss the electrochemical cell performance of the solid-state battery, we use cyclic voltammetry (CV) to evaluate the Sb composite-electrode in two types of battery cells: (i) in an all-solid-state cell with the Li-garnet solid electrolyte and (ii) in a cell with a standard liquid 1 M LPF_6 electrolyte (Fig. 3). The characteristics of the CV measurements reveal several comparable features for the liquid *vs.* the solid-state garnet-type electrolyte and slight differences at peak positions and broadening occur due to the polarization in the solid electrolyte system. Lithiation of Sb by forming alloys of Li_2Sb and Li_3Sb can be measured at 0.9 V and 0.7 V, respectively; during discharge for both kinds of cells at a scan rate of 0.01 mV s^{-1} (see Fig. 3a and b). Numerous earlier *in situ* XRD measurements[78–80] confirm the formation of Li_2Sb and Li_3Sb alloys within the given voltage-range of 0.9 to 0.7 V *vs.* Li^+/Li being also in agreement with theoretical calculations by Huggins.[75] During the charge cycle, Li_3Sb forms pure Sb at about 1.1 V, which is clearly visible from CV curves of the Sb nanoparticle electrodes measured with both solid LLZO electrolyte and also the liquid LPF_6 electrolyte for comparison. Importantly, the high lithiation/de-lithiation potentials (0.7–1.1 V *vs.* Li^+/Li) of antimony indicate a pure alloying mechanism for the processed Sb based anodes with LLZO solid electrolyte that can inherently solve any Li dendrite growth problems even when high current densities are applied to the LLZO/electrode interface for short times.

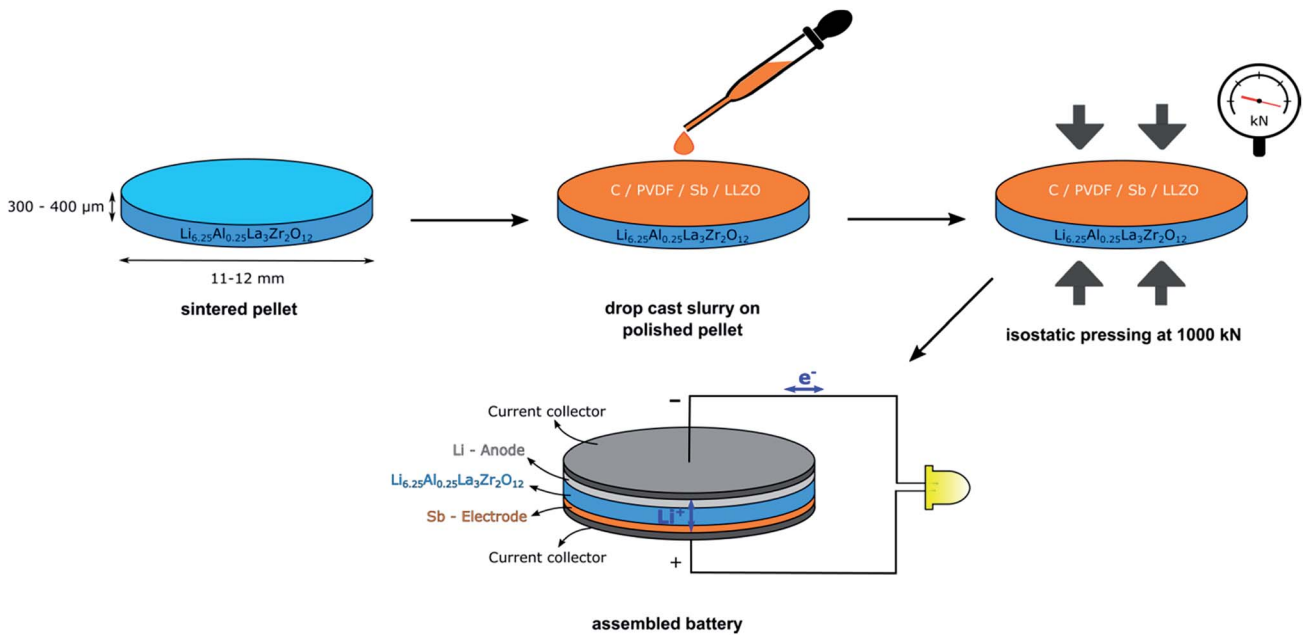

Fig. 1 Schematic process of the electrode slurry deposition and all-solid-state battery assembly based on LLZO electrolyte with nano-Sb composite and Li-metal electrode.

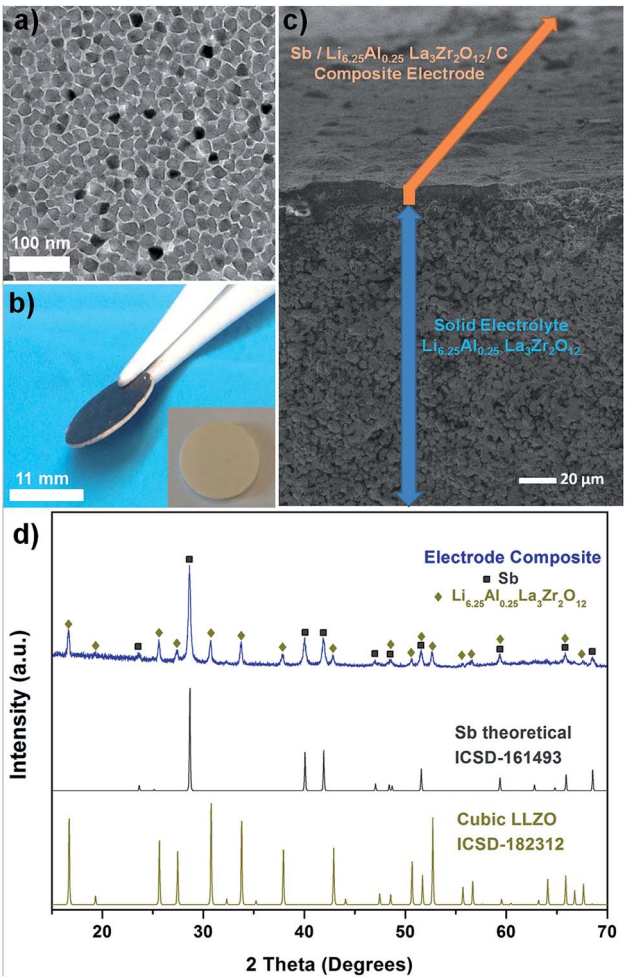

Fig. 2 (a) TEM image of Sb-nanoparticles for electrode fabrication. (b) Sb-based electrode casted onto a LLZO pellet (inset: a plain sintered pellet without any electrode on top). (c) Cross-sectional SEM micrograph of an all-solid-state battery displaying LLZO solid electrolyte and Sb composite electrode layers. (d) XRD powder patterns of Sb based electrode composite (blue), Sb and cubic $Li_7La_3Zr_2O_{12}$ (LLZO).

To explore and estimate the possible performance of all-solid-state batteries under real working conditions they were tested by galvanostatic cycling at various rates and cycling conditions. The galvanostatic charge/discharge curves and the cycling performance of all-solid-state batteries based on nano-Sb and c-$Li_{6.25}Al_{0.25}La_3Zr_2O_{12}$ are displayed in Fig. 4. Sb NPs can be reversibly lithiated and de-lithiated at 0.8 and 1.1 V, respectively, delivering a high storage capacity of 230 mA h g^{-1} and a high coulombic efficiency of 99.9% at a current density of 240 mA g^{-1} for at least 250 cycles (Fig. 4a and b). The cycling stability and the coulombic efficiency are rather remarkable in comparison to similar all-ceramic LLZO based systems previously reported on Li-titanate anodes.[51,81] The electrochemical performance and stability of the solid Li-garnet ceramic cell with integrated antimony electrode are also compared with various standard liquid-based electrolytes such as LiTFSI (Tol/DME), LiBOB (vinylsilane), LiTFSI (tetraglyme) and $LiPF_6$ (EC/DMC) in the field to put the result in perspective. We report that all galvanostatic curves show low over potential and distinct charge/discharge plateaus comparable with tests employing different liquid electrolytes (see ESI Fig. S1a‡). It is important to note that the electrochemical behavior of the Sb electrode with LLZO solid-state electrolyte is superior to liquid-based electrolyte systems, both in terms of higher coulombic efficiency and cycling stability (ESI Fig. S1b and c‡).

We now carefully analyze the storage capacity of the Sb composite anode with LLZO electrolyte which is confirmed to increase up to 330 mA h g^{-1} at a low current density of 40 mA g^{-1} (Fig. 4c and d). Rate capability measurement show that increasing the discharge/charge current rate up to 500 mA g^{-1} does not significantly affect the delivered capacities. In fact, it has been revealed that at 200, 400 and 500 mA g^{-1} current rates, the capacity is almost identical (240–230 mA h g^{-1}), suggesting high Li-ion diffusion and low impeding nature of the Sb composite anode/LLZO interface. Importantly, the capacity of Sb NPs can be fully recovered to its initial value of 330 mA h g^{-1} at lower current rates. Besides, post-mortem analysis of cells after cycling indicate no reaction between c-$Li_{6.25}Al_{0.25}La_3Zr_2O_{12}$ solid electrolyte and the Sb composite electrode or mechanical degradation due to volumetric expansion within the limits of the applied techniques (see ESI Fig. S2‡ for SEM images and EDS spectra of a cell interface cross-section).

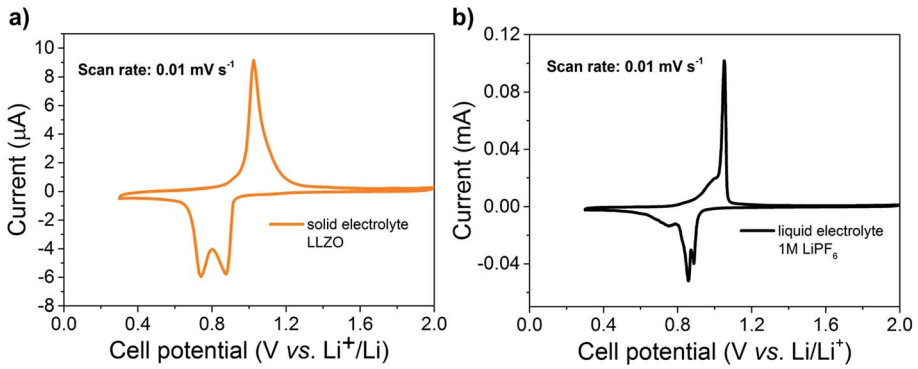

Fig. 3 Comparison of cyclic voltammograms of Sb based electrode between 2.0 and 0.3 V at a scanning rate of 0.01 mV s^{-1} with: (a) all-solid-state battery arrangement with LLZO solid electrolyte. (b) Standard liquid Li-ion battery configuration with 1 M $LiPF_6$ in ethylene carbonate/dimethyl carbonate (1 : 1 vol%) liquid electrolyte.

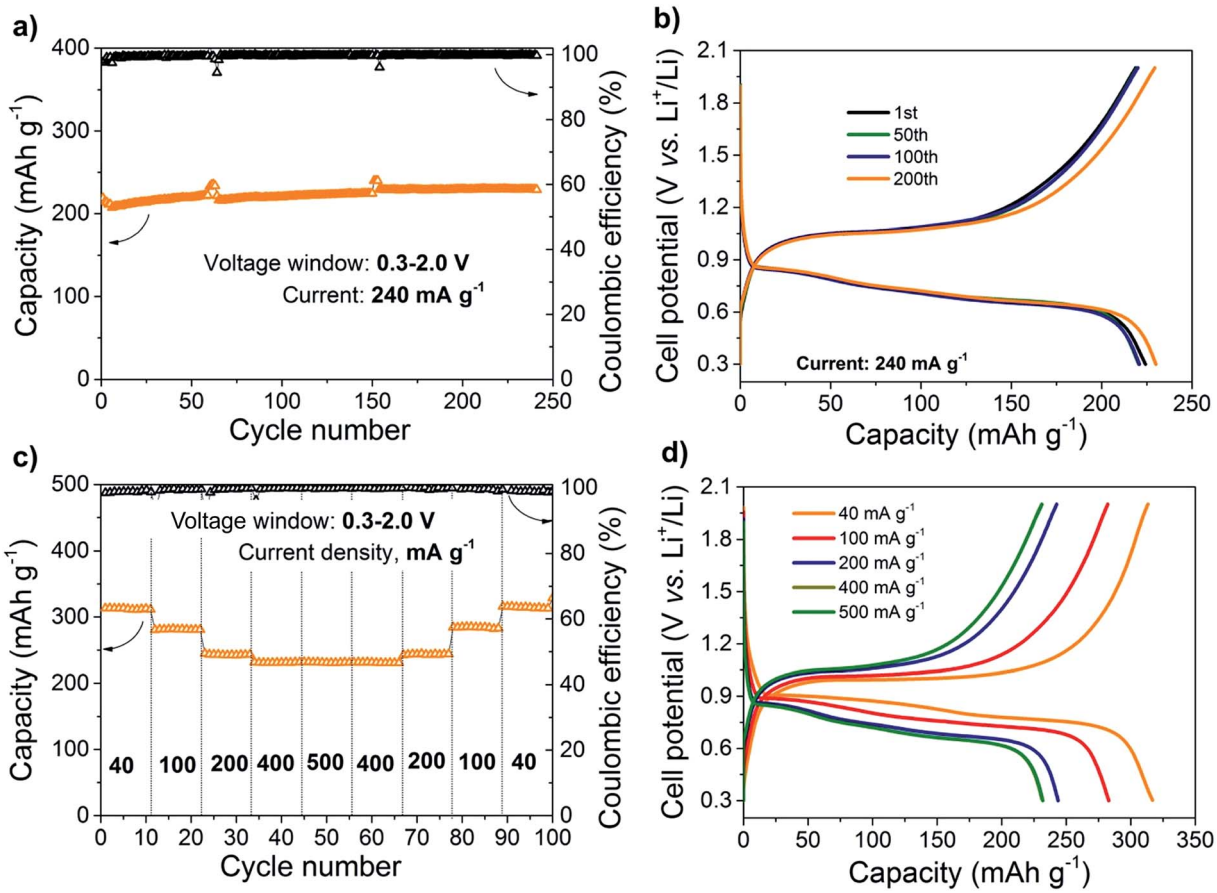

Fig. 4 Galvanostatic cycling measurements of Sb/$Li_{6.25}Al_{0.25}La_3Zr_2O_{12}$ all-solid-state batteries within 0.3–2.0 V at a temperature of 95 °C: (a) capacity *vs.* cycle number and coulombic efficiency measured at 240 mA g^{-1} rate. (b) Charge/discharge curves measured at different cycles. (c) Rate capability at current rates of 40, 100, 200, 400 and 500 mA g^{-1}. (d) Charge/discharge curves measured at variable current rates (1C is equal to 660 mA g^{-1}).

To put these results in perspective, we summarize the performance and characteristics of our all-ceramic battery assembly based on the synthesized c-$Li_{6.25}Al_{0.25}La_3Zr_2O_{12}$ with composite Sb anode and compare those to all-solid-state batteries based on LLZO garnet electrolyte published in literature (Fig. 5 and Table 1). Note that literature examples utilizing liquid electrolytes and other electrolyte salts as additives in the tests of electrodes against LLZO solid electrolytes are excluded herein, as we pursue a full solid-state battery approach here. Based on published discharge capacities and materials used for Li-garnet all-solid-state batteries and new Sb-composite electrodes discussed throughout the work the following conclusions can be drawn. First, the majority of studies published in the literature use and focus on cathode materials, and more specifically on $LiCoO_2$, as the electrode of their all-solid-state battery cells.[11,53,82–84] Second, to reach close-to-theoretical capacities, vacuum-based thin film deposition techniques (*e.g.* pulsed laser deposition) are extensively used for the deposition of the electrode on sintered LLZO electrolyte pellets;[53,83] while other methods such as co-pressing, screen printing, and sol–gel require the addition of additional sintering aids or the addition of liquid electrolyte into the LLZO electrolyte or electrode to produce hybrid systems rather than all-solid-state batteries.[11,82,84] Finally and most notably, the composite Sb-based electrode tested here outperforms other anode

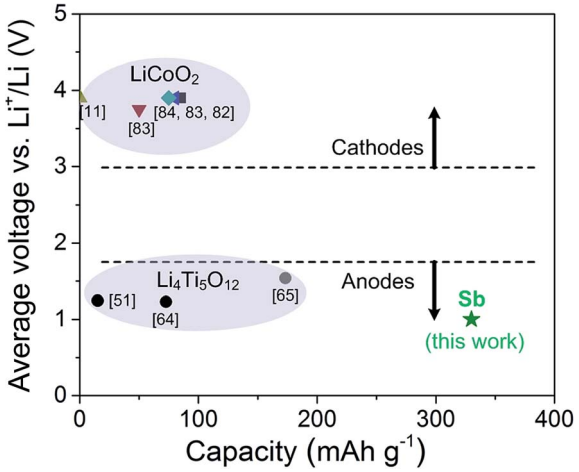

Fig. 5 Discharge capacities of all-solid-state batteries with variously doped cubic $Li_7La_3Zr_2O_{12}$ and different electrode materials from literature.

Table 1 Literature overview of all-solid-state batteries based on garnet electrolytes (mainly from the data points in Fig. 5) showing electrolyte composition, ionic conductivity and density, electrode materials, deposition method, and electrochemical battery performances

Electrolyte			Electrode		Battery performance			
Electrolyte material	Li-ion conductivity (S cm^{-1})	Relative density (%)	Electrode material	Deposition method[a]	Discharge voltage (V)	Discharge capacity (mA h g^{-1})	Multiple cycles (>20)	Ref.
$Li_{6.25}Al_{0.25}La_3Zr_2O_{12}$	5.0×10^{-4}	87	Sb	Slurry coating on sintered pellet assembly	2.0–0.3 V	330 (95 °C)	✗	This work
$Li_{6.25}Al_{0.25}La_3Zr_2O_{12}$	5.0×10^{-4}	87	$Li_4Ti_5O_{12}$	Slurry coating on sintered pellet assembly	1.25	15, 75 (95 °C)	✗	51 and 64
$Li_{6.75}La_3Zr_{1.75}Nb_{0.25}O_{12}$	1.23×10^{-3}	89–92	$LiCoO_2$	Screen printing	3.9	85		82
$Li_7La_3Zr_2O_{12}$ (1.7 wt% Al, 0.1 wt% Si)	6.8×10^{-4}	93	$LiCoO_2$	PLD	3.75	50		83
$Li_7La_3Zr_2O_{12}$ (1.7 wt% Al, 0.1 wt% Si)	6.8×10^{-4}	93	$LiCoO_2$	PLD with Nb interlayer	3.9	80	✗	83
$Li_{6.8}La_{2.95}Ca_{0.05}Zr_{1.75}Nb_{0.25}O_{12}$	4.8×10^{-4}	90	$LiCoO_2$	Co-pressing followed by co-sintering	3.9	75		84
$Li_7La_3Zr_2O_{12}$ (uncontrolled Al doping from crucible)	1.8×10^{-4}	—	$LiCoO_2$	Sol–gel	3.9	0.3		11
$Li_{6.4}Ga_{0.2}La_3Zr_2O_{12}$	5.0×10^{-4}	78–84	$LiMn_{1.5}Ni_{0.5}O_4$	Slurry coating on sintered pellet assembly	—	—		81
$Li_{6.25}Al_{0.25}La_3Zr_2O_{12}$	5.0×10^{-4}	87	$Li_4Ti_5O_{12}$	PLD	1.5	175		65

[a] PLD: pulsed laser deposition.

alternatives such as $Li_4Ti_5O_{12}$ and is a viable choice to be used with Li-garnet solid electrolytes also considering high current outputs drive in and out of the system. Besides, it is important to note that Sb is employed in the form of a composite electrode slurry onto flat LLZO pellet surfaces by direct casting followed by isostatic pressing. All-solid-state batteries of composition Sb/LLZO/Li prepared in this way showed very stable cycling properties at 95 °C and high charge/discharge capacities of up to 330 mA h g^{-1}. The cycling properties are quite remarkable as high capacities of 230 mA h g^{-1} and high coulombic efficiency of 99.9% at 240 mA g^{-1} were delivered for at least 250 cycles. Compared to previous studies as shown in Fig. 5 and Table 1, the superior electrochemical properties reported here for Sb/LLZO/Li all-solid-state batteries can be mainly attributed to the combination of following effects: (i) the utilization of a low dimensional composite of metalloid antimony nanoparticles and LLZO formed through ball-milling, (ii) the careful assembly procedures that are all carried out in Ar-filled glove box preventing any reaction of LLZO solid electrolyte with CO_2 and H_2O,[85] and (iii) the benefits acquired through the isostatic pressing of cells. Specifically, the importance of the last point shows itself in the electrochemical performance of non-pressed cells that deliver rather diminished capacities, poorer cycling properties and low coulombic efficiency, which we also add for comparison to indicate the importance of processing in ESI Fig. S3 and S4.‡ Besides, careful analysis of the AC impedance spectra of all-ceramic battery assembly based on c-$Li_{6.25}Al_{0.25}La_3Zr_2O_{12}$ with nano-Sb anode further verified the improved contacting and reduced resistances for the pressed battery cell arrangement (ESI Fig. S5‡). We also emphasize that development of alternative anode materials for high power density all-solid-state Li-ion batteries is underestimated in respect to the fact that formation of Li dendrites becomes favorable at high current densities exceeding 0.5 mA cm^{-2}. Therefore, even though the formation of Li dendrites can be in principle fully suppressed with highly dense LLZO electrolytes at low current densities, these batteries would have rate capability limitations which limit current integration for electric vehicles with desired charging times of less than an hour. In this context, a composite Sb–LLZO–C anode can be considered as a first choice for high power density SSLIBs, which could ultimately avoid any Li plating/stripping and dendrite formation instabilities.

3. Conclusion

The feasibility of all-solid-state Li-ion batteries based on Li-garnet solid electrolyte in terms of processing, materials and cycling at stable performance with relatively fast rates has been showcased for a metalloid-based anode such as antimony. Ultimately, this finding contributes to the goal to provide the energy storage based on all-solid-state battery cells to deliver high currents without Li-dendrite formation for which we demonstrate high capacities around 230 mA h g^{-1} with high coulombic efficiency of 99.9% at 240 mA g^{-1} at least 250 cycles. Considering the goal of fast charging of batteries, most importantly for electric vehicles, turning to metalloid alloys for the anode may be a viable option to integrate Li-garnet solid-state electrolytes at high safety.

Finding suitable and cheap processing methods is essential to design the battery cells for which, with the example of a metalloid alloy based on Sb nanocrystals, we propose fabrication guidelines of how to obtain electromechanically stable interfaces towards the solid-state Li-garnet by methods suitable for mass manufacturing. It is shown that all-solid-state batteries with no need for any type of liquids prepared in this way exhibit good cycling performance and high charge/discharge capacities of up to 330 mA h g^{-1} at 95 °C. Importantly the capacity and cycling stability achieved exceed other non-lithium anode integration reports for all-solid-state batteries based on fast conducting Li-garnet electrolytes. Both the cycling stability and the coulombic efficiency are notable even surpassing some of the standard liquid electrolytes used in the field. It can be concluded that metalloids such as processed Sb nanoparticles inherently work as a Li alloying/di-alloying electrodes at about 0.7–1.1 V *vs.* Li^+/Li and are by their intrinsic nature a way to avoid Li dendrite formation at high currents. The material stability and engineering guidelines of the cells could result in new opportunities choosing metalloid alloys such as antimony as alternative anodes for all-solid-state batteries with applications in electric vehicles.

4. Experimental section

Synthesis of Sb NPs

To synthesize 20 nm Sb NPs, $NaBH_4$ (48 mmol, 98%, ABCR) was dissolved in distilled *N*-methyl-2-pyrrolidone (NMP, 51 mL, 99.8%, Fluorochem Ltd) in a three-necked flask under nitrogen and heated to 60 °C. $SbCl_3$ (12 mmol, 99%, ABCR) was dissolved in NMP (9 mL) and was quickly injected *via* syringe. The reaction mixture instantly turned black and was immediately cooled down using an ice-water bath. After cooling to room temperature, Sb NPs were separated from the solution by centrifugation (8000 rpm, 4 min) and washed three times with deionized water (30 mL) to remove unreacted $NaBH_4$ and water-soluble side products such as NaCl. The reaction product was finally dried in the vacuum oven at room temperature, yielding 1.2 g of Sb NCs (82% reaction yield). NMP solvent recovered after centrifuging can be reused with or without distillation, giving very similar results.

c-$Li_{6.25}Al_{0.25}La_3Zr_2O_{12}$ solid electrolyte powder synthesis and pellet processing

Sub-micron sized powder of the garnet type c-$Li_{6.25}Al_{0.25}La_3Zr_2O_{12}$ was synthesized by dissolving stoichiometric amounts of $LiNO_3$ (99%, Alfa Aesar), $Al(NO_3)_3\cdot 9H_2O$ (99%, Fluka Chemika), $La(NO_3)_3\cdot 6H_2O$ (99.9%, Alfa Aesar), and zirconium(IV) acetylacetonate (98%, ABCR) in an ethanol–water solvent mixture at 70 °C. The lithium precursor was taken in excess of 10 wt% to compensate for Li-loss during calcination and sintering. The solvent was left to evaporate overnight at 95 °C to receive a dry xerogel. The xerogel was crushed in a mortar and calcined at 650 °C for 15 h under a constant synthetic air flow with a heating/cooling rate of 5 °C min^{-1}, giving the cubic phase of the solid electrolyte $Li_{6.25}Al_{0.25}La_3Zr_2O_{12}$. Solid electrolyte pellets were processed by first pressing green bodies of this powder into cylindrical pellets (1–2 mm thick, 13 mm diameter) by uniaxial pressing at 35 kN followed by isostatic pressing at 1000 kN. After sintering of the green bodies embedded in parent powder at 1070 °C for 10 h under O_2 atmosphere with a heating/cooling rate of 5 °C min^{-1}, dense electrolyte pellets of composition c-$Li_{6.25}Al_{0.25}La_3Zr_2O_{12}$ were obtained. For the assembly of all-solid-state batteries, the sintered pellets were polished with sandpaper (P400/P1200) to a uniform thickness of 360 ± 20 μm. A more detailed description of the steps outlined above can be found in our recent publications using the same LLZO synthesis method and electrolyte pellet processing.[51,64,81]

Cell and composite components

Carbon black (Super C65, TIMCAL), PVDF (poly(vinylidene fluoride), MW ~ 534 000, Aldrich), NMP (99%, Sigma Aldrich), Li foil (MTI Corp.), 1 M solution of $LiPF_6$ in ethylene carbonate/dimethyl carbonate (EC/DMC, Novolyte), Celgard separator (Celgard 2400, 25 μm microporous monolayer polypropylene membrane, Celgard Inc. USA), lass microfiber separator (GF/D, Cat no. 1823-257, Whatman), Cu foil (9 mm, MTI Corporation), coin-type cells (Hohsen Corp., Japan).

Composite Sb–LLZO–C electrode fabrication cell assembly and electrochemical measurements of all-solid-state Li-ion batteries

In a typical electrode preparation, Sb NPs, LLZO electrolyte powder, CB and PVDF binder (40 : 40 : 10 : 10 wt%) were combined with NMP solvent in the glovebox and mixed in a Fritsch Pulverisette 7 classic planetary mill for 1 h at 500 rpm. The slurry was coated onto LLZO sintered pellet then dried overnight at 80 °C under vacuum prior to use. After drying of the electrode layer, the pellet was wrapped into Al-foil in order to protect the thin and porous cathode layer from sticking to the protection rubber used during cold isostatic pressing at 1000 kN (Weber Presse, Germany) for 4 minutes. Final thickness of the Sb based electrode was in the range of 10–15 μm. The pressed pellet was carefully unwrapped and Swagelok-type cells were assembled against Li-metal counter electrodes. All electrochemical measurements were conducted in homemade, reusable and air-tight Swagelok-type cells assembled in an Ar-filled glove box (O_2, 1 ppm, H_2O, 1 ppm). Elemental lithium (Alfa Aesar 0.75 mm Li-metal foil) was employed as both reference and counter electrode. Lithium foils that are cut in matching sizes to the solid electrolyte pellets are mechanically contacted and placed in Swagelok-type cells. Galvanostatic cycling tests were carried out at 95 °C on MPG2 multi-channel workstation (BioLogic) using current density of 0.04–0.5 A g^{-1} (0.018–0.225 mA cm^{-2}) between 0.3–2 V *vs.* Li^+/Li. Capacities were normalized by the mass of antimony active material. We note that for practical applications, further work might be needed, particularly on optimization of the electrode mass-loading for obtaining higher areal capacities as indicated by Albertus *et al.*[86]

Electrochemical impedance spectroscopy (EIS) of Sb/$Li_{6.25}Al_{0.25}La_3Zr_2O_{12}$/Li solid state battery was performed at temperature of 95 °C on a multi-channel potentiostat/galvanostat

(VMP3, from Bio-Logic). The EIS spectra were recorded in the frequency range between 1 MHz and 10 mHz with a perturbation amplitude of 100 mV.

Reference measurements of Sb NPs with various liquid electrolytes

In a typical electrode preparation, Sb NPs, CB and CMC binder (64 : 21 : 15 wt%) were combined with deionized water and mixed in a Fritsch Pulverisette 7 classic planetary mill for 1 h at 500 rpm. The aqueous slurries were coated onto Cu current collectors and then dried overnight at 80 °C under vacuum prior to use. All electrochemical measurements were conducted in coin type cells assembled in an Ar-filled glove box (O_2, 1 ppm, H_2O, 1 ppm). Elemental lithium was employed as both reference and counter electrode. Glass fiber and Celgard were used as separators. Galvanostatic cycling tests were carried out at room temperature on MPG2 multi-channel workstation (Bio-Logic). Capacities were normalized by the mass of active material.

Physical characterization

Transmission Electron Microscopy (TEM) images were obtained with a Philips CM30 TEM microscope at 300 kV using carbon-coated Cu grids as substrates (Ted-Pella). Powder X-ray diffraction (XRD) patterns of the powder samples were recorded using a STOE Stadi P diffractometer equipped with a germanium monochromator and $CuK_{\alpha 1}$ radiation operated at 35 mA and 35 kV. Scanning electron microscopy (SEM) analysis of samples were recorded with a Zeiss Gemini 1530 operated at 5 kV. Energy-dispersive X-ray spectroscopy (EDS) measurements were performed on postmortem cleaved cross-sections of cycled cells with a UltraDry II (Thermo Fisher Scientific) equipped on the SEM.

Conflicts of interest

There are no conflicts to declare.

Acknowledgements

The authors thank the company ALSTOM for financial support and the Competence Center Energy and Mobility (CCEM) and Swisselectrics for funding of the projects: Proposal 911 "All Solid State Li-Ion Batteries based on New Ceramic Li-Ion Electrolytes". J. L. M. Rupp thanks the Thomas Lord Foundation and MIT Skoltech Seed Fund Award 6937431. This research is also a part of the activities of SCCER HaE, which was financially supported by the Innosuisse – Swiss Innovation Agency.

References

1 D. Larcher and J. M. Tarascon, *Nat. Chem.*, 2015, **7**, 19–29.
2 J.-M. Tarascon and M. Armand, in *Materials For Sustainable Energy: A Collection of Peer-Reviewed Research and Review Articles from Nature Publishing Group*, World Scientific, 2011, pp. 171–179.
3 C. M. Hayner, X. Zhao and H. H. Kung, *Annu. Rev. Chem. Biomol. Eng.*, 2012, **3**, 445–471.
4 Y. Wang, W. D. Richards, S. P. Ong, L. J. Miara, J. C. Kim, Y. Mo and G. Ceder, *Nat. Mater.*, 2015, **14**, 1026–1031.
5 J. Li, Y. Cheng, L. Ai, M. Jia, S. Du, B. Yin, S. Woo and H. Zhang, *J. Power Sources*, 2015, **293**, 993–1005.
6 S. S. Zhang, *J. Power Sources*, 2007, **164**, 351–364.
7 X. Ji, K. T. Lee and L. F. Nazar, *Nat. Mater.*, 2009, **8**, 500–506.
8 S. Afyon, M. Worle and R. Nesper, *Angew. Chem., Int. Ed.*, 2013, **52**, 12541–12544.
9 S. Afyon, D. Kundu, A. J. Darbandi, H. Hahn, F. Krumeich and R. Nesper, *J. Mater. Chem. A*, 2014, **2**, 18946–18951.
10 P. L. Moss, R. Fu, G. Au, E. J. Plichta, Y. Xin and J. P. Zheng, *J. Power Sources*, 2003, **124**, 261–265.
11 M. Kotobuki, H. Munakata, K. Kanamura, Y. Sato and T. Yoshida, *J. Electrochem. Soc.*, 2010, **157**, A1076.
12 P. G. Bruce, S. A. Freunberger, L. J. Hardwick and J. M. Tarascon, *Nat. Mater.*, 2012, **11**, 19–29.
13 J. Li, C. Ma, M. Chi, C. Liang and N. J. Dudney, *Adv. Energy Mater.*, 2015, **5**, 1401408.
14 J. F. M. Oudenhoven, L. Baggetto and P. H. L. Notten, *Adv. Energy Mater.*, 2011, **1**, 10–33.
15 T. C. Frankel, *The cobalt pipeline*, 2016.
16 F. W. Wellmer and J. D. Becker-Platen, Global nonfuel mineral resources and sustainability, in *Proceedings for a Workshop on Deposit Modeling, Mineral Resource Assessment, and Their Role in Sustainable Development*, August 2000.
17 Electronic industry citizenship coalition, http://www.eiccoalition.org/.
18 E. A. Olivetti, G. Ceder, G. G. Gaustad and X. Fu, *Joule*, 2017, **1**, 229–243.
19 J. Janek and W. G. Zeier, *Nat. Energy*, 2016, **1**, 16141.
20 N. Kamaya, K. Homma, Y. Yamakawa, M. Hirayama, R. Kanno, M. Yonemura, T. Kamiyama, Y. Kato, S. Hama, K. Kawamoto and A. Mitsui, *Nat. Mater.*, 2011, **10**, 682–686.
21 R. Kanno and M. Murayama, *J. Electrochem. Soc.*, 2001, **148**, A742–A746.
22 Y. Seino, T. Ota, K. Takada, A. Hayashi and M. Tatsumisago, *Energy Environ. Sci.*, 2014, **7**, 627–631.
23 W. D. Richards, L. J. Miara, Y. Wang, J. C. Kim and G. Ceder, *Chem. Mater.*, 2016, **28**, 266–273.
24 S. Wenzel, S. Randau, T. Leichtweiß, D. A. Weber, J. Sann, W. G. Zeier and J. Janek, *Chem. Mater.*, 2016, **28**, 2400–2407.
25 B. R. Shin, Y. J. Nam, D. Y. Oh, D. H. Kim, J. W. Kim and Y. S. Jung, *Electrochim. Acta*, 2014, **146**, 395–402.
26 Y. S. Jung, D. Y. Oh, Y. J. Nam and K. H. Park, *Isr. J. Chem.*, 2015, **55**, 472–485.
27 X. Liang, Q. Pang, I. R. Kochetkov, M. S. Sempere, H. Huang, X. Sun and L. F. Nazar, *Nat. Energy*, 2017, **2**, 17119.
28 A. Sakuda, N. Nakamoto, H. Kitaura, A. Hayashi, K. Tadanaga and M. Tatsumisago, *J. Mater. Chem.*, 2012, **22**, 15247–15254.
29 Y. Seino, T. Ota and K. Takada, *J. Power Sources*, 2011, **196**, 6488–6492.

30 N. Ohta, K. Takada, I. Sakaguchi, L. Zhang, R. Ma, K. Fukuda, M. Osada and T. Sasaki, *Electrochem. Commun.*, 2007, **9**, 1486–1490.
31 C. Yada, A. Ohmori, K. Ide, H. Yamasaki, T. Kato, T. Saito, F. Sagane and Y. Iriyama, *Adv. Energy Mater.*, 2014, **4**, 1301416.
32 T. Thompson, S. Yu, L. Williams, R. D. Schmidt, R. Garcia-Mendez, J. Wolfenstine, J. L. Allen, E. Kioupakis, D. J. Siegel and J. Sakamoto, *ACS Energy Lett.*, 2017, **2**, 462–468.
33 R. Murugan, V. Thangadurai and W. Weppner, *Angew. Chem.*, 2007, **46**, 7778–7781.
34 V. Thangadurai, S. Narayanan and D. Pinzaru, *Chem. Soc. Rev.*, 2014, **43**, 4714–4727.
35 J. L. Allen, J. Wolfenstine, E. Rangasamy and J. Sakamoto, *J. Power Sources*, 2012, **206**, 315–319.
36 H. Buschmann, J. Dolle, S. Berendts, A. Kuhn, P. Bottke, M. Wilkening, P. Heitjans, A. Senyshyn, H. Ehrenberg, A. Lotnyk, V. Duppel, L. Kienle and J. Janek, *Phys. Chem. Chem. Phys.*, 2011, **13**, 19378–19392.
37 L. Cheng, J. S. Park, H. Hou, V. Zorba, G. Chen, T. Richardson, J. Cabana, R. Russo and M. Doeff, *J. Mater. Chem. A*, 2014, **2**, 172–181.
38 I. N. David, T. Thompson, J. Wolfenstine, J. L. Allen and J. Sakamoto, *J. Am. Ceram. Soc.*, 2015, **98**, 1209–1214.
39 R. Djenadic, M. Botros, C. Benel, O. Clemens, S. Indris, A. Choudhary, T. Bergfeldt and H. Hahn, *Solid State Ionics*, 2014, **263**, 49–56.
40 A. Düvel, A. Kuhn, L. Robben, M. Wilkening and P. Heitjans, *J. Phys. Chem. C*, 2012, **116**, 15192–15202.
41 W. Gu, M. Ezbiri, R. P. Rao, M. Avdeev and S. Adams, *Solid State Ionics*, 2015, **274**, 100–105.
42 N. Janani, C. Deviannapoorani, L. Dhivya and R. Murugan, *RSC Adv.*, 2014, **4**, 51228–51238.
43 Y. Jin and P. J. McGinn, *J. Power Sources*, 2011, **196**, 8683–8687.
44 D. Rettenwander, P. Blaha, R. Laskowski, K. Schwarz, P. Bottke, M. Wilkening, C. A. Geiger and G. Amthauer, *Chem. Mater.*, 2014, **26**, 2617–2623.
45 S. Afyon, F. Krumeich and J. L. M. Rupp, *J. Mater. Chem. A*, 2015, **3**, 18636–18648.
46 C. Bernuy-Lopez, W. Manalastas, J. M. Lopez del Amo, A. Aguadero, F. Aguesse and J. A. Kilner, *Chem. Mater.*, 2014, **26**, 3610–3617.
47 H. El Shinawi and J. Janek, *J. Power Sources*, 2013, **225**, 13–19.
48 M. A. Howard, O. Clemens, E. Kendrick, K. S. Knight, D. C. Apperley, P. A. Anderson and P. R. Slater, *Dalton Trans.*, 2012, **41**, 12048–12053.
49 D. Rettenwander, C. A. Geiger, M. Tribus, P. Tropper and G. Amthauer, *Inorg. Chem.*, 2014, **53**, 6264–6269.
50 M. Kotobuki, K. Kanamura, Y. Sato and T. Yoshida, *J. Power Sources*, 2011, **196**, 7750–7754.
51 J. van den Broek, S. Afyon and J. L. M. Rupp, *Adv. Energy Mater.*, 2016, **6**, 1600736.
52 L. Cheng, W. Chen, M. Kunz, K. Persson, N. Tamura, G. Chen and M. Doeff, *ACS Appl. Mater. Interfaces*, 2015, **7**, 2073–2081.
53 S. Ohta, T. Kobayashi, J. Seki and T. Asaoka, *J. Power Sources*, 2012, **202**, 332–335.
54 M. A. Huang, T. Liu, Y. F. Deng, H. X. Geng, Y. Shen, Y. H. Lin and C. W. Nan, *Solid State Ionics*, 2011, **204**, 41–45.
55 W. Luo, Y. Gong, Y. Zhu, K. K. Fu, J. Dai, S. D. Lacey, C. Wang, B. Liu, X. Han and Y. Mo, *J. Am. Chem. Soc.*, 2016, **138**, 12258–12262.
56 X. Han, Y. Gong, K. K. Fu, X. He, G. T. Hitz, J. Dai, A. Pearse, B. Liu, H. Wang and G. Rubloff, *Nat. Mater.*, 2017, **16**, 572.
57 W. Luo, Y. Gong, Y. Zhu, Y. Li, Y. Yao, Y. Zhang, K. Fu, G. Pastel, C. F. Lin and Y. Mo, *Adv. Mater.*, 2017, **29**, 1606042.
58 L. Porz, T. Swamy, B. W. Sheldon, D. Rettenwander, T. Frömling, H. L. Thaman, S. Berendts, R. Uecker, W. C. Carter and Y. M. Chiang, *Adv. Energy Mater.*, 2017, **7**, 1701003.
59 F. Aguesse, W. Manalastas, L. Buannic, J. M. Lopez del Amo, G. Singh, A. Llordés and J. Kilner, *ACS Appl. Mater. Interfaces*, 2017, **9**, 3808–3816.
60 C.-L. Tsai, V. Roddatis, C. V. Chandran, Q. Ma, S. Uhlenbruck, M. Bram, P. Heitjans and O. Guillon, *ACS Appl. Mater. Interfaces*, 2016, **8**, 10617–10626.
61 R. Sudo, Y. Nakata, K. Ishiguro, M. Matsui, A. Hirano, Y. Takeda, O. Yamamoto and N. Imanishi, *Solid State Ionics*, 2014, **262**, 151–154.
62 K. Ishiguro, Y. Nakata, M. Matsui, I. Uechi, Y. Takeda, O. Yamamoto and N. Imanishi, *J. Electrochem. Soc.*, 2013, **160**, A1690–A1693.
63 Y. Suzuki, K. Kami, K. Watanabe, A. Watanabe, N. Saito, T. Ohnishi, K. Takada, R. Sudo and N. Imanishi, *Solid State Ionics*, 2015, **278**, 172–176.
64 J. van den Broek, J. L. M. Rupp and S. Afyon, *J. Electroceram.*, 2017, 1–7, DOI: 10.1007/s10832-017-0079-9.
65 R. Pfenninger, S. Afyon, I. Garbayo, M. Struzik and J. L. Rupp, *Adv. Funct. Mater.*, 2018, 1800879.
66 M. He, K. Kravchyk, M. Walter and M. V. Kovalenko, *Nano Lett.*, 2014, **14**, 1255–1262.
67 M. He, M. Walter, K. V. Kravchyk, R. Erni, R. Widmer and M. V. Kovalenko, *Nanoscale*, 2015, **7**, 455–459.
68 K. Kravchyk, L. Protesescu, M. I. Bodnarchuk, F. Krumeich, M. Yarema, M. Walter, C. Guntlin and M. V. Kovalenko, *J. Am. Chem. Soc.*, 2013, **135**, 4199–4202.
69 M. I. Bodnarchuk, K. V. Kravchyk, F. Krumeich, S. Wang and M. V. Kovalenko, *ACS Nano*, 2014, **8**, 2360–2368.
70 S. Wang, M. He, M. Walter, F. Krumeich, K. V. Kravchyk and M. V. Kovalenko, *Nanoscale*, 2018, **10**, 6827–6831.
71 M. Walter, S. Doswald, F. Krumeich, M. He, R. Widmer, N. P. Stadie and M. V. Kovalenko, *Nanoscale*, 2018, **10**, 3777–3783.
72 N. Nitta and G. Yushin, *Part. Part. Syst. Charact.*, 2014, **31**, 317–336.
73 A. Mukhopadhyay and B. W. Sheldon, *Prog. Mater. Sci.*, 2014, **63**, 58–116.
74 M. F. Oszajca, M. I. Bodnarchuk and M. V. Kovalenko, *Chem. Mater.*, 2014, **26**, 5422–5432.
75 J. Wang, I. D. Raistrick and R. A. Huggins, *J. Electrochem. Soc.*, 1986, **133**, 457–460.

76 K. C. Hewitt, L. Y. Beaulieu and J. R. Dahn, *J. Electrochem. Soc.*, 2001, **148**, A402–A410.
77 M. Walter, R. Erni and M. V. Kovalenko, *Sci. Rep.*, 2015, **5**, 8418.
78 C. Villevieille, M. Ebner, J. L. Gómez-Cámer, F. Marone, P. Novák and V. Wood, *Adv. Mater.*, 2015, **27**, 1676–1681.
79 J. L. Gomez-Camer, C. Villevieille and P. Novak, *J. Mater. Chem. A*, 2013, **1**, 13011–13016.
80 I. Devos, M. Womes, M. Heilemann, J. Olivier-Fourcade, J.-C. Jumas and J. L. Tirado, *J. Mater. Chem.*, 2004, **14**, 1759–1767.
81 C. Hansel, S. Afyon and J. L. M. Rupp, *Nanoscale*, 2016, **8**, 18412–18420.
82 S. Ohta, S. Komagata, J. Seki, T. Saeki, S. Morishita and T. Asaoka, *J. Power Sources*, 2013, **238**, 53–56.
83 T. Kato, T. Hamanaka, K. Yamamoto, T. Hirayama, F. Sagane, M. Motoyama and Y. Iriyama, *J. Power Sources*, 2014, **260**, 292–298.
84 S. Ohta, J. Seki, Y. Yagi, Y. Kihira, T. Tani and T. Asaoka, *J. Power Sources*, 2014, **265**, 40–44.
85 W. Xia, B. Xu, H. Duan, X. Tang, Y. Guo, H. Kang, H. Li and H. Liu, *J. Am. Ceram. Soc.*, 2017, **100**, 2832–2839.
86 P. Albertus, S. Babinec, S. Litzelman and A. Newman, *Nat. Energy*, 2017, 1.